A crystal plasticity based investigation of fretting fatigue in bioresorbable magnesium elastic stable intramedullary nails (ESINs)

Enda L. Boland, Parvin Ebrahimi, Elizabeth A. Gallagher, J. Patrick McGarry

School of Engineering, National University of Ireland Galway

Abstract
In this paper, the effect of pitting corrosion on fatigue life and fretting fatigue of elastic stable intramedullary nails (ESINs) is investigated. To this end, using a crystal plasticity formulation, the behaviour of magnesium under large deformations is investigated by implementing a user defined material subroutine (UMAT) in the Abaqus/Standard finite element solver. Using data provided by SEM images, the approximate configurations of grains in the polycrystalline material are obtained. Adopting Mg-RE (73-2) as one of candidates for implant applications, the fatigue analysis is performed, and the results are compared to the experimental fatigue data for various strain amplitudes. Furthermore, the effect of pitting corrosion on the fatigue life of the material is investigated. It is shown that the maximum accumulated plastic slip occurs at the tip of a corrosion pit. This suggests a faster crack initiation rate on corroded magnesium specimens compared to non-corroded ones, under cyclic loading. Application of pitting corrosion before cyclic loading, causes a significant reduction in the predicted cycles to crack initiation, compared to the uncorroded case. However, the number of cycles to crack initiation is almost the same irrespective of the amount of mass loss due to corrosion. Next, by modelling the fretting fatigue of ESINs, it is demonstrated that plastic slip accumulates at both the contact surface and deeper into the grain microstructure. However, the maximum values of stress and accumulated plastic slip occur at the contact surface. While the grain geometry and orientation influence the location and magnitude of accumulated plastic slip. By modelling the fretting fatigue of the material with different amounts of corrosion, it is shown that the maximum accumulated plastic slip occurs at the contact surface for the case without corrosion, and also for different percentages of corrosion. Finally, the results of fretting fatigue simulation of ESINs show that corrosion significantly accelerates crack initiation due to fretting wear.

---

1. Introduction

The use of magnesium (Mg) alloys, which have bioresorbable properties under physiological loading conditions, will address issues with the long-term invasive nature of the current metallic devices such as the need for secondary surgery, mismatched mechanical properties and potentially toxic metal particulates (Zhao et al., 2017). Secondary or revision surgery to remove implants accounts for up to 30% of all elective orthopaedic procedures (Kirchhoff et al., 2008), therefore the bioresorbable properties of Mg where the resorption bi-products are also biocompatible is an extremely desirable clinical feature. Elemental Mg is inadequate for use in structural application due to its low Young’s modulus, limited cold work formability, toughness, limited high strength and creep resistance at elevated temperature, and its poor corrosion resistance (Mordike and Ebert, 2001). Most Mg alloy products are fabricated by high pressure die casting, a high production rate technique capable of producing components with highly accurate dimensions and smooth surface finish (Das, 2008; Froes et al., 1998; Kulekci, 2008; Mordike and Ebert, 2001). The drawback of high pressure die casting and other Mg casting techniques are casting defects and mechanical properties unsuitable for future lightweight applications. Wrought Mg alloys offer better mechanical properties and fatigue properties than cast Mg alloys due to fine grain refinement achieved during thermo-mechanical processing (Shahzad and Wagner, 2009). It is also widely known that wrought Mg alloys exhibit strongly anisotropic plastic deformation behavior under cyclic loading, thus restricting their use in current applications. To overcome the anisotropic behavior of wrought Mg alloys, several techniques have been employed to influence and enrich the properties of Mg-based materials. Improvement in the extrudability and ductility can be achieved through the controlling of grain size and texture development/modification (Mishra et al., 2008). Addition of rare-earth elements (RE) is known to randomize the texture in Mg and reduce anisotropic cyclic behavior while enhancing both monotonic and cyclic properties (Li et al., 2016; F. Mirza et al., 2013; F. A. Mirza et al., 2013; Mirza et al., 2014; Mirza and Chen, 2014; Wang et al., 2013).

The use of Mg alloys is expanding into structural and implant domains, where components are subjected to cyclic loading. It is thus crucial to evaluate the fatigue properties of wrought Mg alloys. In the biomedical field, implants are not only exposed to large cyclic stresses and strains, but also to a corrosive environment. The combination of cyclic loading and corrosion generates damaging phenomena such as corrosion-fatigue (Teoh, 2000). Fretting fatigue can occur when two materials in contact under a normal load are subjected to a cyclic tangential force. This is a concern for biomedical implants such as elastic stable intramedullary nails (ESINs). ESINs are implanted into the intramedullary cavity of the femur or other appropriate long bones of the body as a fracture fixation technique for paediatric patients. The technique was originally introduced as it allowed for a shorter periods of bed rest and earlier weight bearing compared to traction (Ligier et al., 1988). More recently, it is preferred by some surgeons over fixation with screws and plates as the insertion procedure is minimally invasive and does not required stripping of the soft tissue at the fracture site (Narayanan et al., 2004; Nørgaard et al., 2018). ESINs can be subject to cyclical contact forces due to the dynamic loading conditions which may lead to fretting fatigue and crack formation of the ESIN.

Several computational models have been developed to simulate the behavior of biodegradable materials. Using the crystal plasticity framework, the behavior of magnesium stents with HCP crystal structure has been predicted by Grogan et al. (Grogan et al., 2014). A phenomenological corrosion model was also proposed by Grogan et al. (Grogan et al., 2011), to predict the behavior of bioresorbable stents in the presence of corrosion,. The finite element modelling of crack initiation during fretting of stainless steel with FCC crystal structure is performed by McCarthy et al. (McCarthy et al., 2014a, 2013, 2011). Using crystal plasticity formulation, the fretting fatigue crack nucleation in Ti–6Al–4V, with a combination of BCC and HCP crystal structures, has been further investigated by McCarthy et al (McCarthy et al., 2014b).

It should be noted that the simultaneous effects of pitting corrosion and fretting fatigue on the performance of implants has not been considered by previous models. The objective of this paper is to investigate the performance of magnesium ESINs when subjected to fatigue loading, fretting and corrosion. To this end, the crystal plasticity modelling for magnesium HCP crystal, considering microstructure-sensitive crack initiation formulation and the effect of pitting corrosion, is presented in Section 2. Material parameter identification is explained in Section 3. Different results related to cyclic loading and fretting fatigue of ESINs are outlined in Section 4. Section 5 represents some conclusions based on the computational simulations.

2. Modelling framework

2.1. Constitutive modelling of magnesium alloy in the framework of crystal plasticity

The model proposed by Grogan et al. (Grogan et al., 2014) is adopted here to predict the behaviour of magnesium in finite deformation regimes. Based on multiplicative decomposition, the deformation gradient tensor is divided into elastic, $\boldsymbol{F}^e$, and plastic, $\boldsymbol{F}^p$, parts. The extensive explanations of the relations used for crystal plasticity formulations can be found in (Grogan et al., 2014; McGarry et al., 2004, 2007).

$$\boldsymbol{F} = \boldsymbol{F}^e \cdot \boldsymbol{F}^p \qquad (1)$$

The elastic part, containing rigid body motions, is described by an elastic strain energy potential. The prescribed linear relation between Cauchy stress tensor and elastic logarithmic strain tensor can be obtained by Young's modulus E and Poisson's ratio ν.

Considering α as the number of slip systems in magnesium HCP crystal structure, the plastic velocity gradient tensor can be expressed by:

$$\dot{\boldsymbol{F}}^p \cdot \boldsymbol{F}^{p^{-1}} = \sum_\alpha \dot{\gamma}^{(\alpha)} \boldsymbol{s}_\alpha \boldsymbol{m}_\alpha \tag{2}$$

Where $\dot{\gamma}^{(\alpha)}$ is the plastic slip rate for the αth slip system. $\boldsymbol{s}_\alpha$ and $\boldsymbol{m}_\alpha$ are unit vectors describing slip direction and slip plane normal for the αth slip system, respectively.

Schmidt's law is used to describe the plastic slip in magnesium. The rate of plastic shear strain, $\dot{\gamma}^{(\alpha)}$, for the αth slip system is assumed to be dependent on the Schmidt resolved shear stress, $\tau^{(\alpha)}$, acting on that system. A power-law rate-dependent relationship is used to describe the evolution of plastic shear strain.

$$\dot{\gamma}^{(\alpha)} = \dot{a} \operatorname{sgn}\left(\tau^{(\alpha)}\right) \left\{ \left| \frac{\tau^{(\alpha)}}{g^{(\alpha)}} \right| \right\}^n \tag{3}$$

where $\dot{a}$ is the reference strain rate, and n is a material parameter controlling the rate sensitivity of plastic slip, known as rate sensitivity exponent. The evolution equation for the slip system strain hardness, $g^{(\alpha)}$, is such that:

$$\dot{g}^{(\alpha)} = \sum_\alpha h_{\alpha\beta} \left| \dot{\gamma}^{(\beta)} \right| \tag{4}$$

where $h_{\alpha\beta}$ is the strain hardening modulus; $h_{\alpha\alpha}$ and $h_{\alpha\beta}$ ($\alpha \neq \beta$) are the self and latent hardening moduli, respectively.

The hardening moduli are selected such that (Grogan et al., 2014):

$$\begin{aligned} h_{\alpha\alpha} &= h(\gamma_a) \\ h_{\alpha\beta} &= q_{\alpha\beta} h(\gamma_a) \end{aligned} \tag{5}$$

where $q_{\alpha\beta}$ is a set of interaction parameters and γ_a is the accumulated plastic slip, described by:

$$\gamma_a = \sum_\alpha \int_0^t \left| \dot{\gamma}^{(\alpha)} \right| dt \tag{6}$$

where t denotes time and the summation is over all active slip systems at a given material point.

Based on the active slip systems, three different hardening laws are applied for the magnesium crystals (Graff et al., 2007):

$$h(\gamma_a) = h_0 \qquad \text{(Linear hardening)} \tag{7}$$

$$h(\gamma_a) = h_0 \left(1 - \frac{g_0}{g_\infty}\right) exp\left(-\frac{h_0 \gamma_a}{g_\infty}\right) \qquad \text{(Voce hardening)} \tag{8}$$

$$h(\gamma_a) = \begin{cases} h_0 & \text{for} \quad \gamma_a \leq \gamma_{ref} \\ h_0 \left(\frac{\gamma_a}{\gamma_{ref}}\right)^{m-1} & \text{for} \quad \gamma_a > \gamma_{ref} \end{cases} \quad \text{(Deformation twinning)} \tag{9}$$

where h_0 is the initial hardening modulus of slip system, g_0 and g_∞ are initial and maximum strengths of slip system, respectively. γ_{ref} and m are material parameters to be calibrated.

To ensure that activation of twinning is restricted to tensile loading, the following condition is also enforced on the twinning slip systems:

$$g^{(\alpha)} \to \infty \quad \text{for} \quad \tau^{(\alpha)} \leq 0 \tag{10}$$

The material behaviour is implemented in a user defined material subroutine (UMAT) in the Abaqus/Standard finite element solver. In order to simulate the behaviour of HCP crystals considering the effect of twinning, the UMAT subroutine presented by Huang for FCC crystals (Huang, 1991) is modified by Grogan et al. (Grogan et al., 2014).

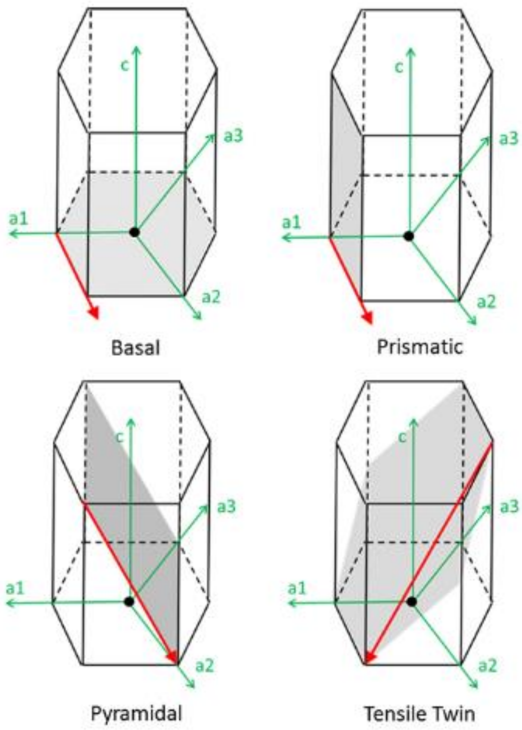

Fig. 1. Demonstration of slip planes and slip directions for different slip systems in the magnesium HCP lattice. Directions are shown in terms of Miller indices, depicted by 'ai' and 'c' axes (Grogan et al., 2014).

As shown in Fig. 1, slip in magnesium is considered to take place on basal $\{0001\}$ and prismatic $\{1\bar{1}00\}$ planes in the <11$\bar{2}$0> directions and in the pyramidal planes $\{11\bar{2}2\}$ in the <11$\bar{2}$3>

directions, where Miller-Bravais indices are assumed. Tensile twinning is also represented as slip on the $\{10\bar{1}2\}$ planes in the <$10\bar{1}1$> directions (Graff et al., 2007). Hardening on the basal systems is assumed to follow Eq. 7, hardening on the prismatic and pyramidal systems is assumed to follow Eq. 8 and hardening on the twinning systems is assumed to follow Eq. 9. Values of latent hardening coefficients, $q_{\alpha\beta}$, are based on previous studies (Graff et al., 2007; Grogan et al., 2014).

2.2. Pitting corrosion of magnesium alloy

Grogan el al. (Grogan et al., 2011) developed a phenomenological pitting corrosion model for biodegradable magnesium alloys implemented for use in computational finite element software, such as Abaqus. Detailed descriptions of the pitting corrosion model can be found in Grogan et al. (Grogan et al., 2011) and Boland et al. (Boland et al., 2018, 2016).

Considering magnesium corrosion as a surface-based phenomenon, the elements on the exterior surface of the material would be exposed to the corrosive environment and are selected as part of the corrosion surface. The phenomenological pitting corrosion model is based on continuum damage mechanics and adopts a scalar damage parameter D ($0 \leq D \leq 1$) to account for the corrosion process. The mechanical properties of the elements on the corrosion surface will be linearly reduced as the damage parameter, D, increases. For a completely damaged element ($D \approx 1$), the element is deleted, and the corrosion surface is then updated to include neighbouring elements via an element connectivity map. The damage evolution law for uniform corrosion, which results in a homogeneous corrosion process, is as follows:

$$\frac{dD}{dt} = \frac{\delta_U}{L_e} k_U \tag{11}$$

where δ_U and L_e are the respective material and FE model characteristic lengths and k_U is the corrosion kinetic parameter. For the uniform case and for a given δ_U and L_e, the damage evolution law is proportional to k_U.

The pitting corrosion model is obtained by the inclusion of a dimensionless pitting parameter, λ_e, in the uniform corrosion model (Grogan et al., 2011):

$$\frac{dD}{dt} = \frac{\delta_U}{L_e} \lambda_e k_U \tag{12}$$

Using a Weibull distribution-based random number generator, each element on the corrosion surface is initially assigned a random pitting parameter, λ_e. Elements on the corrosion surface with larger assigned numbers are more susceptible to pitting corrosion. By the complete degradation and subsequent deletion of an element on the corrosion surface, a pit growth rate parameter, β, controls the rate of neighbouring element degradation such that:

$$\lambda_e = \beta \lambda_n \tag{13}$$

where λ_n is the pitting parameter of the fully degraded element and β is a dimensionless parameter that controls the acceleration/deceleration of pit growth.

In order to account for the stochastic nature of pit locations, each corrosion simulation is done five times with different initial pit configurations. The reported results of this paper are the averaged results of the corresponding five simulations. To this end, different initial seed values are entered into the Weibull distribution based random number generator each time to generate five different initial pit configurations.

2.3. Microstructure-sensitive crack initiation model

In order to predict the number of cycles prior to crack initiation, a microstructure-sensitive methodology developed by Manonukul and Dunne (Manonukul and Dunne, 2004), and used by McCarthy et al. (McCarthy et al., 2014b) is implemented here. The accumulated plastic slip, p, is considered as the controlling parameter for crack initiation which is defined such that (McCarthy et al., 2014b):

$$\dot{p} = \left(\frac{2}{3} L^p : L^p\right)^{1/2} \;\; ; \;\; p = \int_0^t \dot{p}\,dt \tag{14}$$

where L^p denotes the plastic velocity gradient tensor, presented in Eq. (2).

Crack initiation is deemed to occur once p reaches a critical value, p_{crit}, which is determined experimentally from the number of cycles to crack initiation, N_i, and the maximum accumulated plastic slip in one cycle, p_{cyc} . Due to the predicted rapid stabilisation of p with respect to the number of fatigue cycles, N, it is possible to determine p_{crit} from the following equation:

$$p_{crit} = N_i p_{cyc} \tag{15}$$

3. Material parameter identification

3.1. CP model calibration

In order to approximate the microstructure of grains in the material, SEM image of hot extruded Mg-RE (73-2) which is shown in Fig. 2(a) has been used (McGhee, 2017). Addition of RE is known to randomize the texture in Mg and reduce anisotropic cyclic behavior while enhancing both monotonic and cyclic properties (Li et al., 2016; F. Mirza et al., 2013; F. A. Mirza et al., 2013; Mirza et al., 2014; Mirza and Chen, 2014; Wang et al., 2013). Therefore, random orientations are assigned to different grains in the polycrystalline material. The pitting corrosion model has been calibrated using in-vitro corrosion experiments of Mg WE43 alloy (Boland et al., 2018). It should be noted that the Mg-RE (73-2) alloy which is used for simulations in this paper contains rare earth alloying elements, similar to the Mg WE43 alloys.

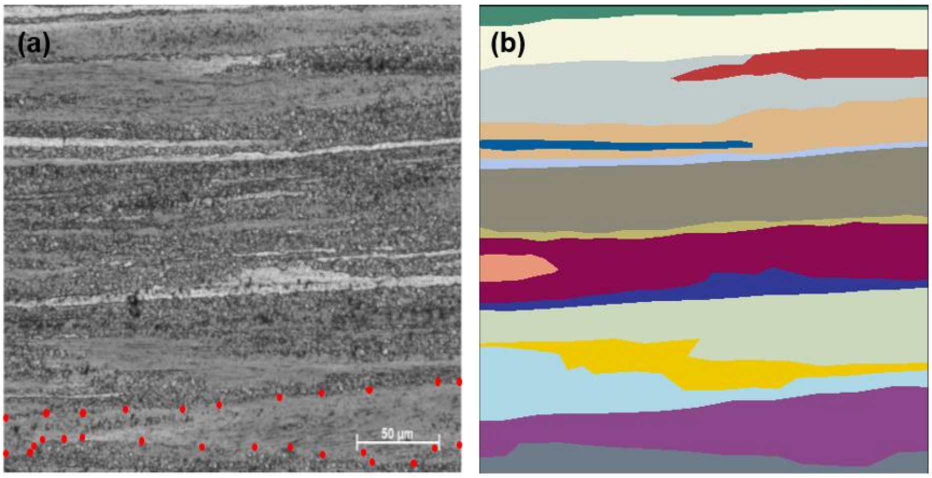

Fig. 2. (a) SEM image of microstructure of hot extruded Mg-RE (73-2) (McGhee, 2017) (b) Approximated grain geometry used for the computational simulations.

The uniaxial tensile test data of Mg-RE (73-2) (McGhee, 2017), is used to calibrate the hardening parameters of the model by an iterative approach. The experimental uniaxial tensile data and the equivalent fitted computational simulation, to calibrate the hardening parameters are shown in Fig. 3. The Von-Mises stress distribution at the end of loading for the simulated material is shown in Fig. 4. The values of the calibrated parameters related to Eqs. (7)-(9), are presented in Table 1.

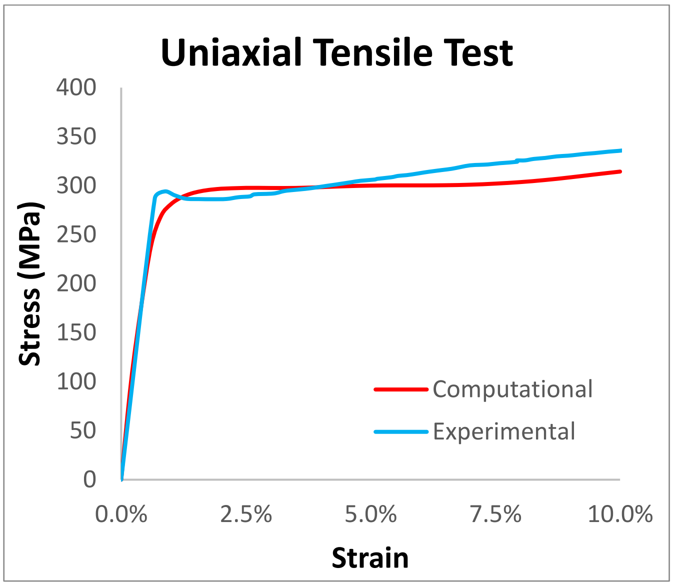

Fig. 3. Comparison of the experimental (McGhee, 2017) and simulated computational results for uniaxial tensile tests

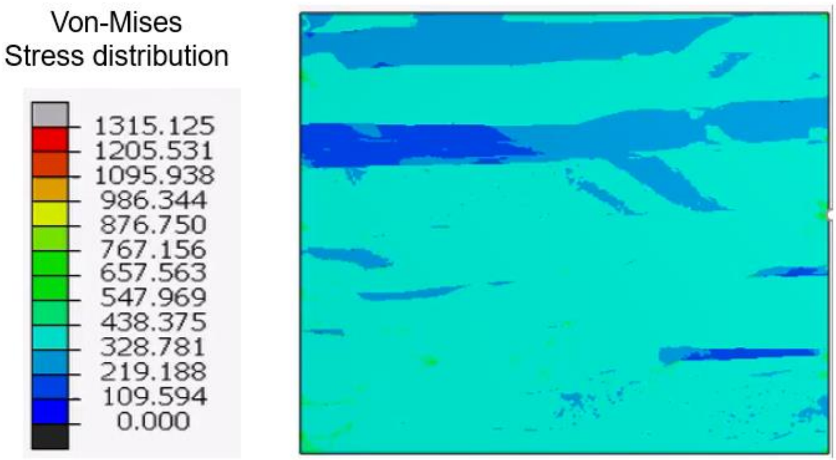

Fig. 4. Von-Mises stress distribution at the end of loading for tensile loading of the simulated material.

Table 1. Material hardening parameters calibrated using experimental results of Mg-RE 73-2.

Parameter	Basal	Prismatic	Pyramidal	Twinning
$\boldsymbol{g_0}$	130	80	160	48
$\boldsymbol{g_\infty}$	0	90	170	0
$\boldsymbol{h_0}$	1	1	1	1

Table 2 represents the magnitudes of interaction coefficients, $q_{\alpha\beta}$, for magnesium single crystals.

Table 2. Latent hardening (interaction) coefficients, $q_{\alpha\beta}$, for magnesium single crystals (Graff et al., 2007; Grogan et al., 2014), where the hardening in slip system α depends on slip in slip system β.

	Basal $\boldsymbol{\beta}$	Prismatic $\boldsymbol{\beta}$	Pyramidal $\boldsymbol{\beta}$	Twinning $\boldsymbol{\beta}$
Basal $\boldsymbol{\alpha}$	$q_{\alpha\beta} = 0.2$	$q_{\alpha\beta} = 0.5$	$q_{\alpha\beta} = 0.5$	$q_{\alpha\beta} = 0.5$
Prismatic $\boldsymbol{\alpha}$	$q_{\alpha\beta} = 0.2$	$q_{\alpha\beta} = 0.2$	$q_{\alpha\beta} = 0.2$	$q_{\alpha\beta} = 0.5$
Pyramidal $\boldsymbol{\alpha}$	$q_{\alpha\beta} = 1.0$	$q_{\alpha\beta} = 1.0$	$q_{\alpha\beta} = 0.2$	$q_{\alpha\beta} = 0.25$
Twinning $\boldsymbol{\alpha}$	$q_{\alpha\beta} = 1.0$	$q_{\alpha\beta} = 1.0$	$q_{\alpha\beta} = 0.2$	$q_{\alpha\beta} = 0.25$

3.2.The crack initiation model calibration

It should be noted that for determining the critical accumulated slip, we must know when the crack initiation occurs, which is not always easy to determine. However, in general, it is easy to determine the number of cycles to failure. Consequently, if the number of cycles to crack initiation is much larger than that for propagation, we can equate the critical accumulated slip for crack initiation with the accumulated slip to cause failure. Therefore, by having the number of cycles to failure, N_f, and by calculating the accumulated plastic slip per cycle, p_{cyc}, the critical accumulated slip, p_{crit}, can be calculated (Manonukul and Dunne, 2004).

The experimental low cycle fatigue data for Mg-RE (73-2) which is presented in Fig. 5, represents the relationship between total strain amplitude, $\Delta\varepsilon$, and number of cycles to failure, N_f (Mcghee, 2017). The value of p_{crit} describing microstructural crack initiation for Mg-RE (73-2), is then identified to be equal to 2.848 using the N_f value corresponding to one particular value of strain amplitude. Using the obtained value of p_{crit} and Eq. (15), the low-cycle fatigue response for our simulation is plotted for the range of applied strain amplitudes in Fig. 5.

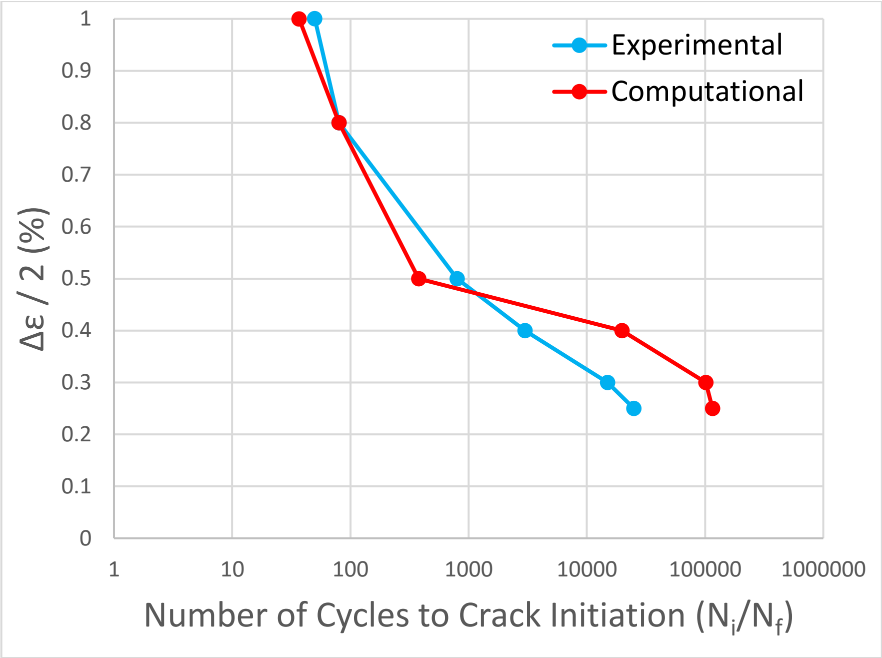

Fig. 5. Experimental (Mcghee, 2017) and predicted total strain amplitude vs. number of cycles to failure for Mg-RE (73-2)

4. Results and discussions

4.1. Fatigue analysis neglecting the effect of corrosion

To examine the accuracy of calibrated parameters, the fatigue analysis is performed and the results are compared to the experimental fatigue data of Mg-RE (73-2) (Mcghee, 2017). The applied loadings and boundary conditions to the material are shown in Fig. 6. The left and bottom edges are prevented from moving in x and y directions, respectively. Using equation constraints, the top and right faces are forced to remain horizontal and vertical, respectively. In order to simulate low-cycle fatigue, a cyclic displacement is applied to the right edge. Four-noded plane strain elements are used throughout this work.

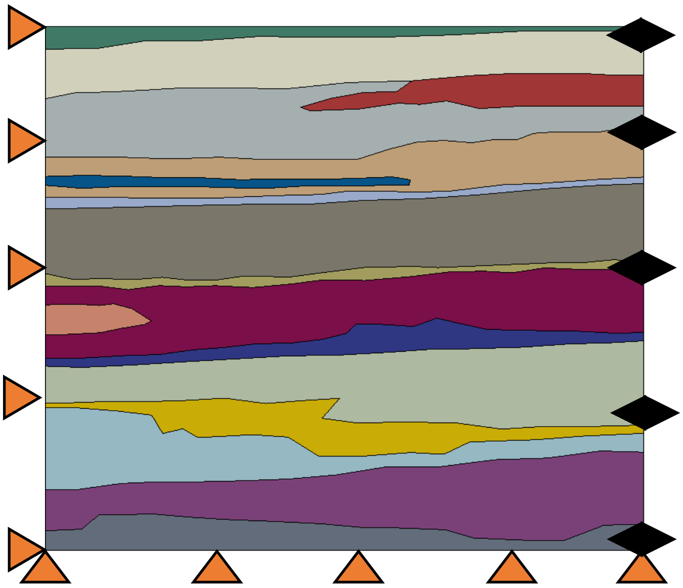

Fig. 6. Demonstration of loadings and boundary conditions used for simulating fatigue failure of material in Abaqus software.

The comparison of computational and experimental stress-strain curves for ± 1 % and ± 0.75 % strain amplitudes, in the first cycle and mid-life cycles are shown in Figs. 7 and 8, respectively.

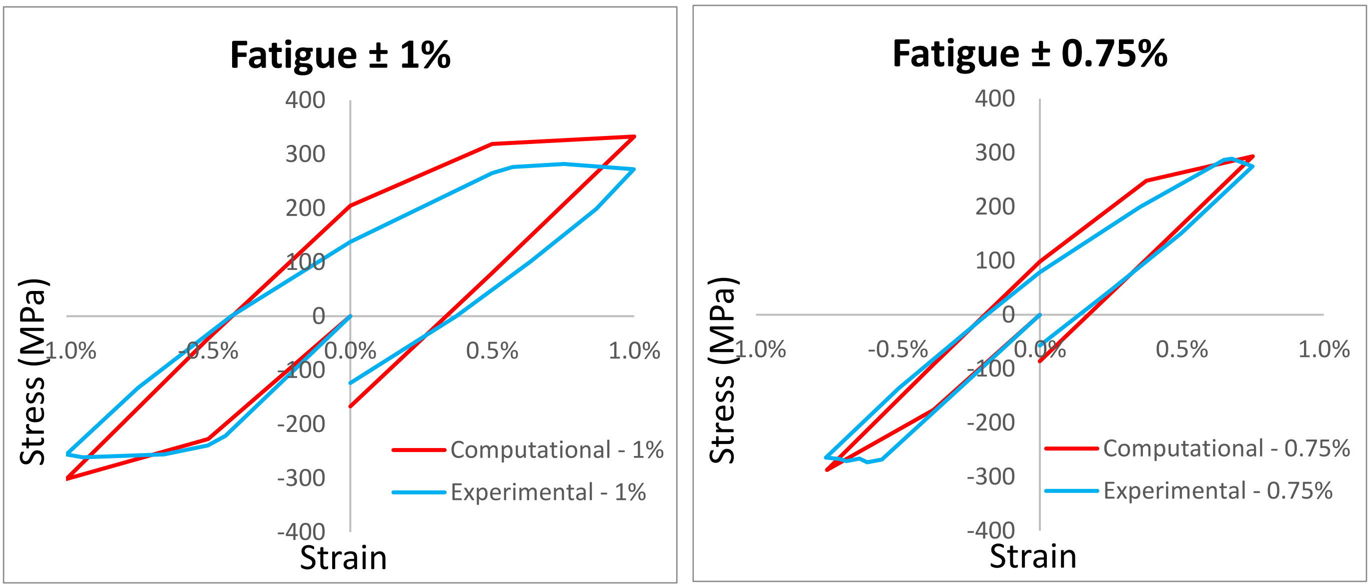

Fig. 7. Comparison of computational and experimental (Mcghee, 2017) stress-strain responses of Mg-RE (73-2) at strain amplitudes of ± 1 % and ± 0.75 % in the 1st cycle.

In Fig. 7 we see that the computational model predicts a very good fit with the experimental results for the first cycle of the fatigue test for both strain amplitudes shown. For the mid-life cycles shown in Fig. 8, the computational model deviates slightly from the experimental results, however the overall shape of the hysteresis curves matches the experiments quite well.

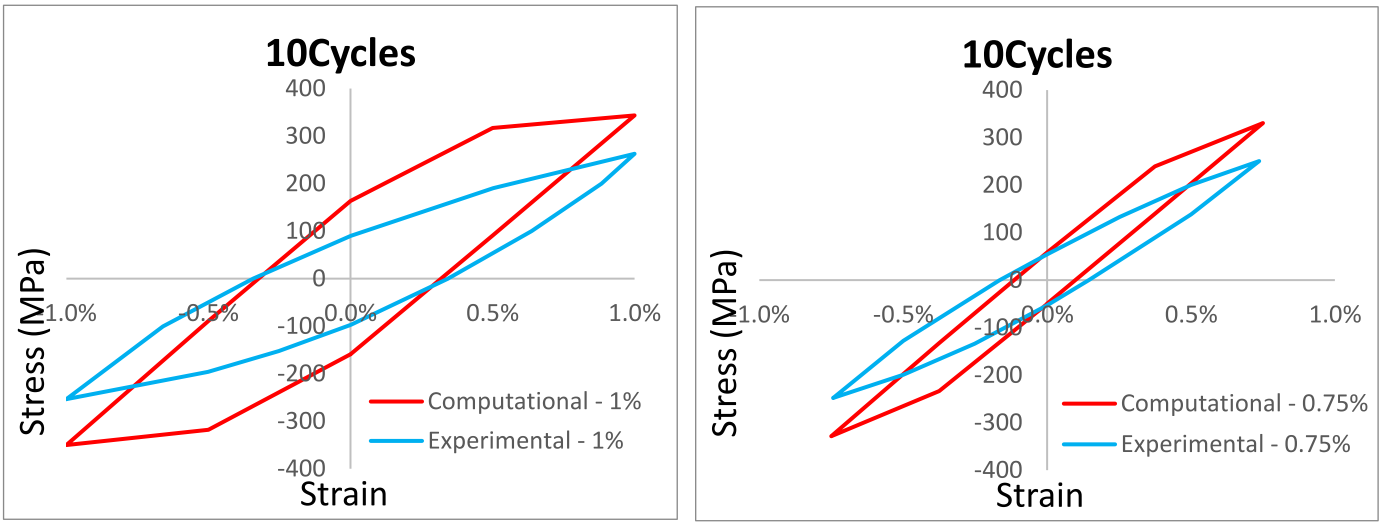

Fig. 8. Comparison of computational and experimental (Mcghee, 2017) stress-strain responses of Mg-RE (73-2) at strain amplitudes of ± 1 % and ± 0.75 % in the mid-life cycle.

The accumulated plastic slip distribution at the end of 1st and 10th cycles for ±1% strain amplitude is shown in Fig. 9. The increase in plastic slip predicted with increasing number of cycles is clearly evident.

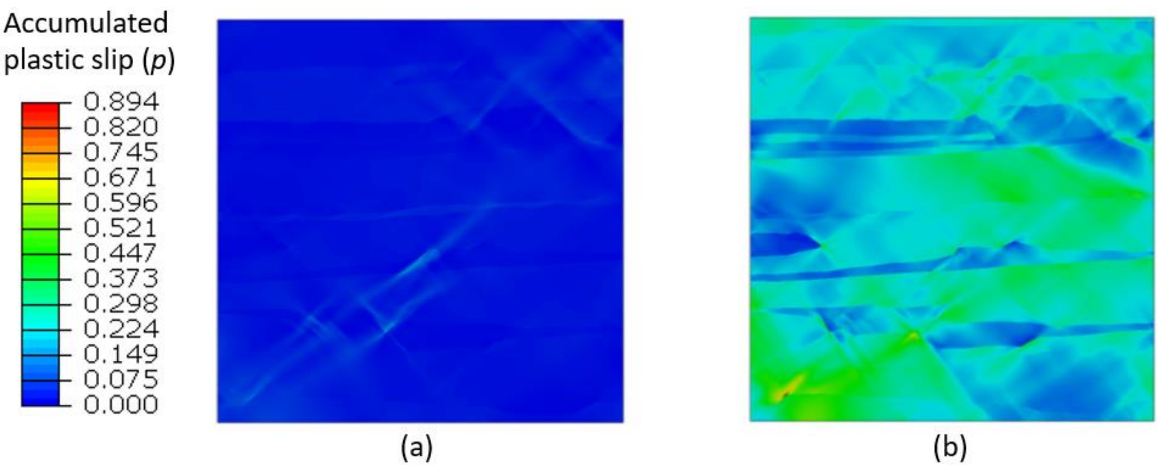

Fig. 9. distribution of accumulated plastic slip for strain amplitude of ±1% at the end of (a) 1st, and (b) 10th cycle

4.2. Fatigue analysis by considering the effect of pitting corrosion

The grain geometry and material described previously is also used for modelling the pitting corrosion with crystal plasticity formulation. The pitting corrosion model is applied to the top and bottom surfaces in accordance with the experimental fatigue results/observations reported in (McCarthy et al., 2013). Following corrosion, a cyclic load is applied to the material geometry as shown in Fig. 6, to investigate the effects of mass loss due to corrosion and strain range on the fatigue life of the samples. The contour plots of accumulated plastic slip for different amounts of mass loss due to corrosion after 10 cycles is shown in Fig. 10.

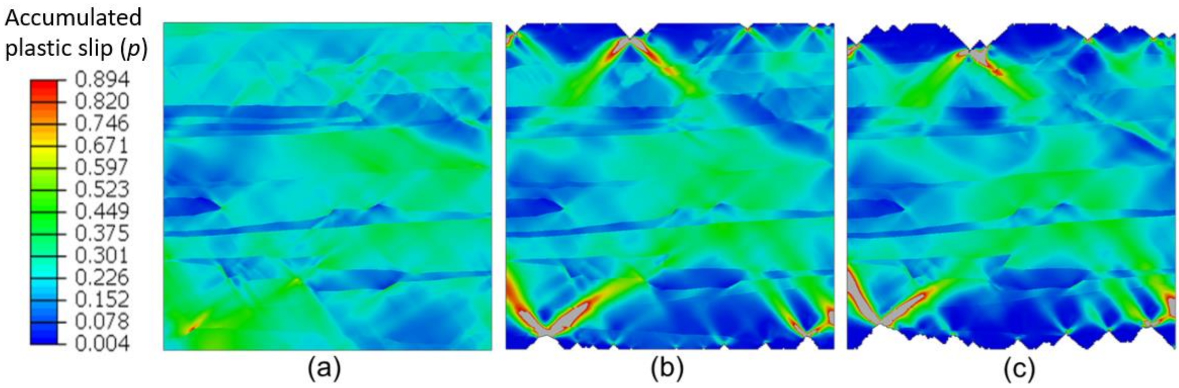

Fig. 10. Contour plots showing the accumulated plastic slip (p) after 10 cycles with ±1 % strain applied for (a) no corrosion, (b) 1% mass loss due to corrosion, and (c) 5% mass loss due to corrosion.

In Fig(a), the maximum accumulated plastic slip of 0.89 with ±1 % applied strain occurs in the bottom left of an uncorroded sample. This is the predicted location of crack initiation due to cyclical fatigue. In contrast to the uncorroded sample (Fig. 10(a)), both corroded samples predict the maximum accumulated plastic slip occurs at the tip of a corrosion pit, as shown in the contour plots in Fig(b) andFig(c) for 1% mass loss and 5% mass loss, respectively. In the case of ±1% applied strain, the average maximum accumulated plastic slips for 1%, 2%, 5% and 10% mass losses are 6.58, 6.57, 7.44, and 6.74, respectively. This suggests that when subjected to cyclical fatigue loading, cracks initiate at a faster rate on corroded magnesium specimens compared to non-corroded/uncorroded samples.

The computational curves of applied strain versus number of cycles to crack initiation, for different amounts of mass loss due to corrosion, are plotted in Fig. 11.

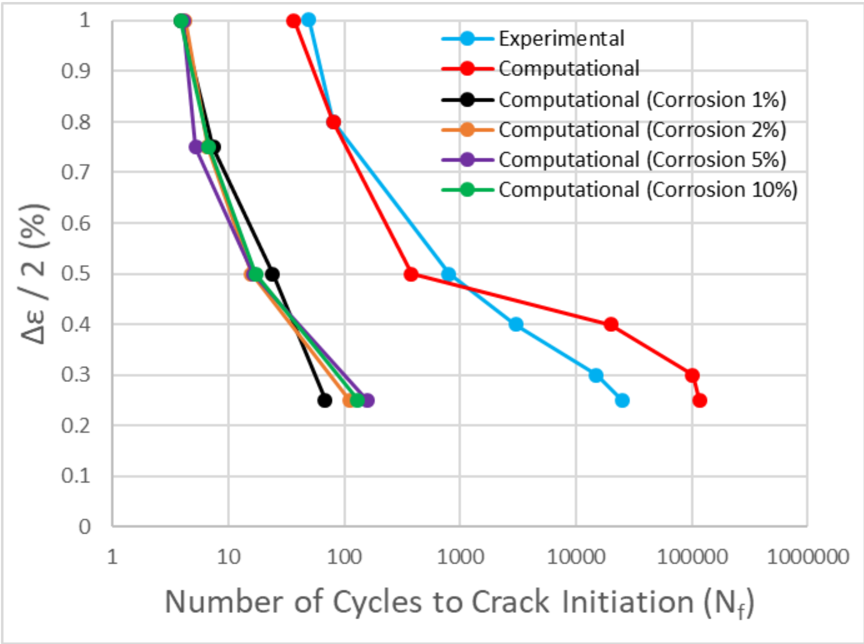

Fig. 11. Experimental (Mcghee, 2017) and computational curves of applied strain versus number of cycles to crack initiation, for different amounts of mass loss due to corrosion.

As previously mentioned, the computational model with no corrosion is calibrated with the experimental data, and a value of 2.848 for p_{crit} is obtained. As demonstrated by Fig. , the calibrated computational model accurately replicates the experimental data at strain ranges of 0.5% to 1%. However, the cycles to failure is overpredicted for strain ranges of 0.25% to 0.4%. Applying pitting corrosion to the model before application of cyclical fatigue loading significantly reduces the predicted cycles to crack initiation for all simulated strain ranges as illustrated in Fig. . However, increasing quantities of mass loss due to corrosion (1%, 2%, 5% and 10%) have minimal effect on the predicted cycles to crack initiation.

4.3.Fretting fatigue analysis

Due to contact between the two implanted ESINs, fretting fatigue is a probable failure/damage mechanism. A FE model of a cylinder-on-flat fretting configuration based on the experimental work of Ding et al. (Ding et al., 2009), and computational work of McCarthy et al. (McCarthy et al., 2014b, 2011) is implemented to investigate fretting fatigue. The schematic of fretting fatigue model is demonstrated in Fig. 12.

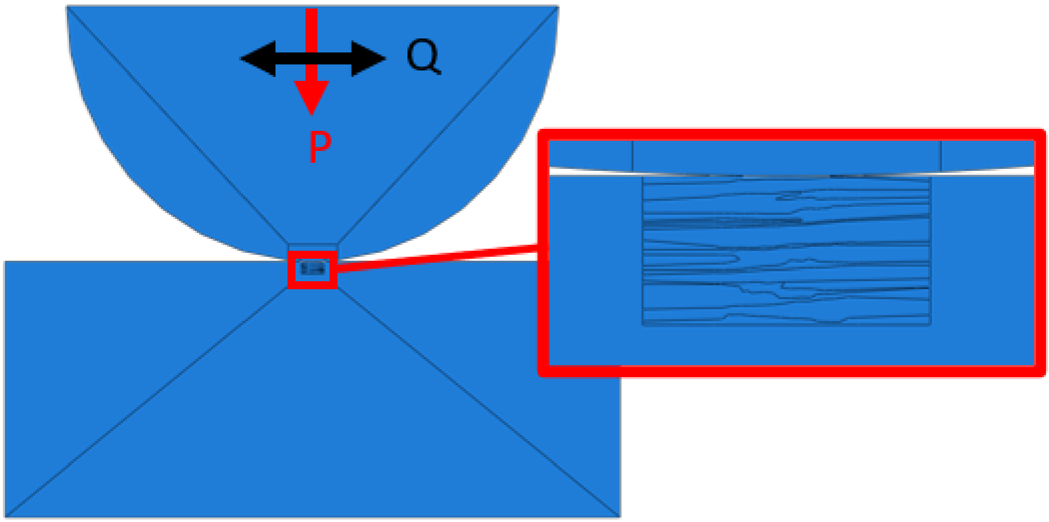

Fig. 12. A schematic of the fretting fatigue FE model, highlighting the contact zone

The values of normal load, P, and tangential displacement, Q, are obtained from ESIN implantation simulation. The contour plot of contact stress between two implanted ESINs is shown in Fig. 13. The contact stress of 35 MPa predicted by the ESIN simulation translates to a normal load of 210 N and displacement of 2 μm in the fretting fatigue model. These values have been implemented in all further fretting fatigue results in this section, unless otherwise stated.

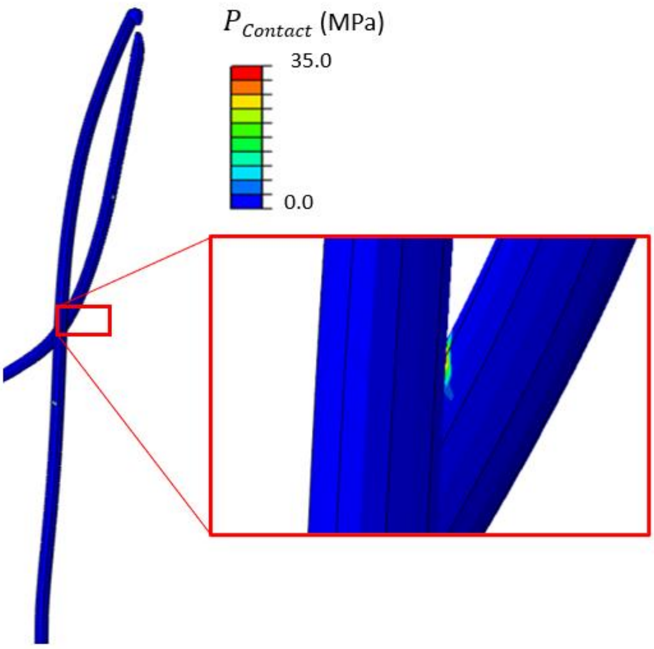

Fig. 13. contour plot of contact stress between two implanted ESINs

The contour plots of Von-Mises stress and accumulated plastic slip for fretting fatigue of uncorroded magnesium after the 10th cycle are shown in Fig. 14. It is predicted that the maximum values of stress and accumulated plastic slip occur at the contact surface. However, significant values of plastic slip also accumulate deeper into the grain microstructure. It should be noted that the grain geometry and orientation influence the location and magnitude of accumulated plastic slip.

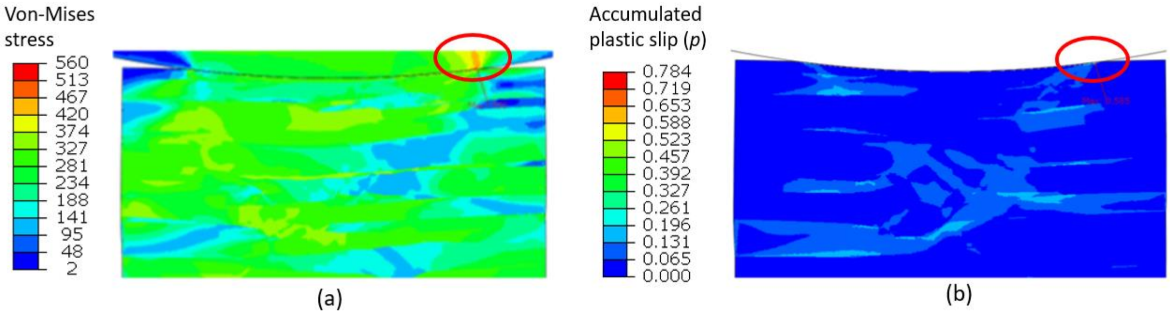

Fig. 14. Contour plots of (a) Von-Mises stress, and (b) accumulated plastic slip for fretting fatigue of material with no corrosion with normal load of 220 N and tangential displacement of 2 μm at the end of the 10th cycle.

Fig. 15 demonstrates the distribution of accumulated plastic slip in the magnesium alloy. The results are related to 10th cycle with normal load of 210 N and tangential displacement of 2 μm. As depicted in Fig. 15, plastic slip accumulates at both the contact surface and deeper into the grain microstructure. It should be noted that the grain geometry and orientation influence the location and magnitude of accumulated plastic slip.

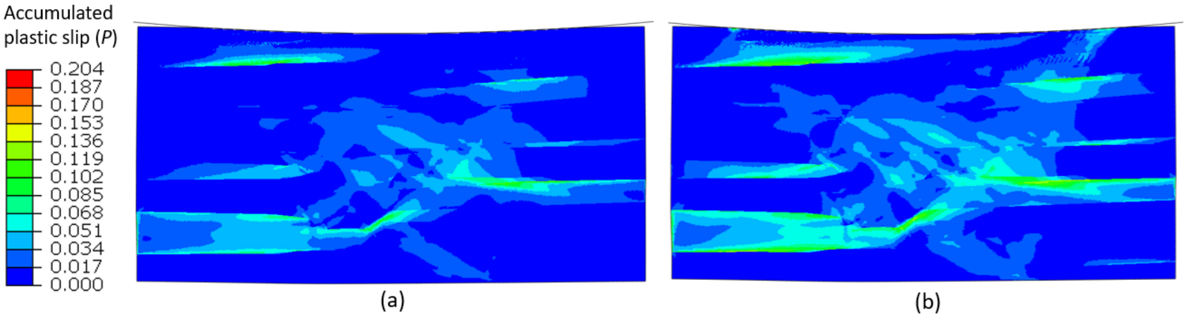

Fig. 15. Contour plot of the accumulated plastic slip parameter in the magnesium alloy: (a) before and (b) after 10 cycles with a normal load of 210 N and tangential displacement of 2 μm.

In order to investigate the effect of corrosion on fretting fatigue of the material, the fretting analysis is done for different amounts of mass loss due to corrosion. Fig. 16 (a), (b) and (c) shows the accumulated plastic slip contour plots for samples with no corrosion, 3.5% corrosion and 8.5% corrosion, respectively. The maximum accumulated plastic slip occurs at the contact surface in all three cases. It can be seen that any increase in mass loss due to corrosion causes an increase in the maximum accumulated plastic slip. By increasing the corrosion, a more localized accumulated plastic slip is observed.

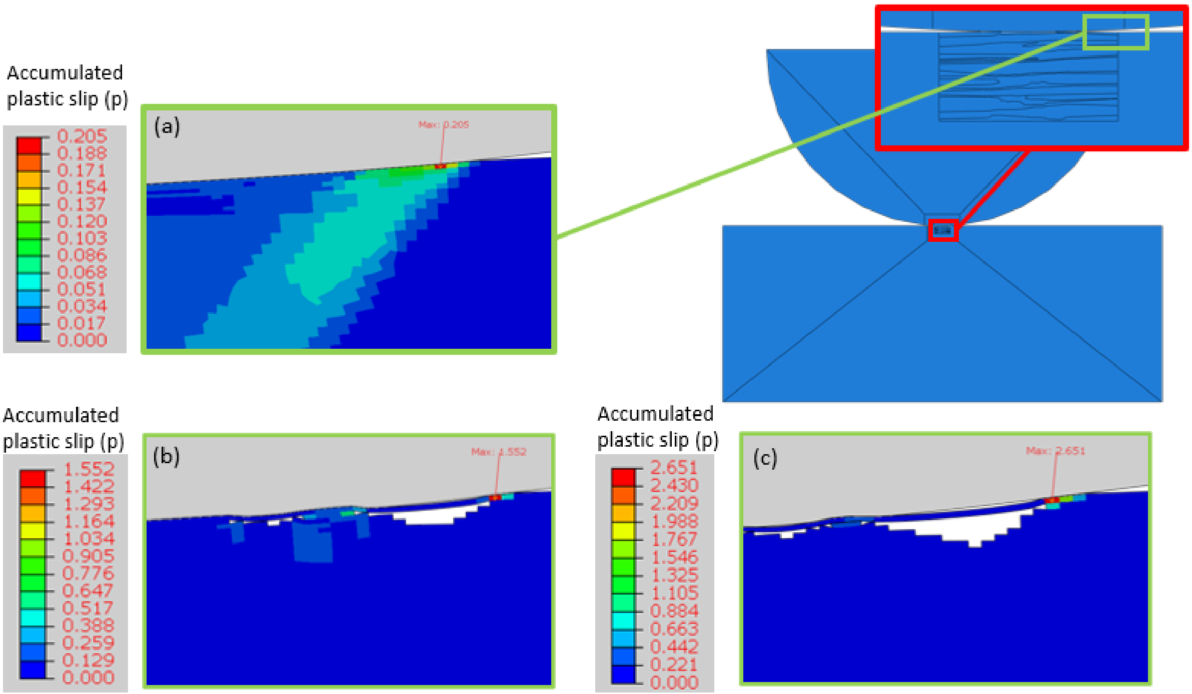

Fig. 16. contour plots of accumulated plastic slip in the enlarged area for different amounts of corrosion: (a) no corrosion, (b) 3.5% corrosion, (c) 8.5% corrosion, with normal load of 220 N and tangential displacement of 2 μm.

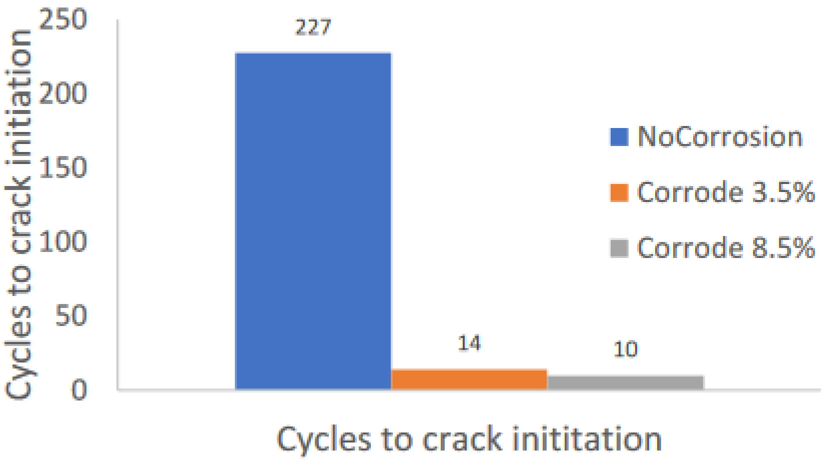

Fig. 17. comparison of number of cycles to crack initiation for 3 different simulations with no corrosion, 3.5% corrosion and 8.5% corrosion with normal load of 220 N and tangential displacement of 2 μm.

Fig. 17. shows the number of cycles to crack initiation for 3 different simulations: no corrosion, 3.5% corrosion and 8.5% corrosion with normal load of 220 N and tangential displacement of 2 μm. It is clear that corrosion also accelerates crack initiation due to fretting.

5. Conclusions

Using the crystal plasticity formulation, the behaviour of magnesium under large deformations is investigated by implementing a user defined material subroutine (UMAT) in the Abaqus/Standard finite element solver. Considering a microstructure-sensitive crack initiation formulation and the effect of pitting corrosion, the cyclic and fretting fatigue behaviour of a Mg alloy is investigated. Using data provided by SEM images, the approximate configurations of grains in the polycrystalline material are obtained. In order to investigate the effects of pitting corrosion and fretting fatigue on the overall behaviour of the material, different simulations have been performed. Reasonable agreement is obtained by comparing the results of fatigue analysis with the available experimental data of Mg-RE (73-2) (Mcghee, 2017). The effect of different amounts of mass-loss due to pitting corrosion on the response of the material is investigated. It is shown that the tip of corrosion pits would be the critical points and when subjected to cyclical fatigue loading, cracks initiate at a faster rate on corroded magnesium specimens compared to non-corroded ones. Furthermore, it is shown that applying pitting corrosion to the model before application of cyclical fatigue loading significantly reduces the predicted cycles to crack initiation. However, the different quantities of mass loss due to corrosion has minimal effect on the predicted cycles to crack initiation. The results of fretting fatigue simulations show the accumulation of plastic slip at both the contact surface and deeper into the grain microstructure. Considering different percentages of corrosion at the contact surface of ESINs, it is demonstrated that by any increase in corrosion, the number of cycles to crack initiation will decrease.

References

Boland, E.L., Kelly, N., Sweeney, C.A., 2016. A Review of Material Degradation Modelling for the Analysis and Design of Bioabsorbable Stents Lipostent View project Computational and Experimental Investigation of the Degradation of Poly-L-lactide (PLLA) for the Design of a Biodegradable Polymeric Sten. Springer. https://doi.org/10.1007/s10439-015-1413-5

Boland, E.L., Shirazi, R.N., Grogan, J.A., McHugh, P.E., 2018. Mechanical and Corrosion Testing of Magnesium WE43 Specimens for Pitting Corrosion Model Calibration. Adv. Eng. Mater. 20, 1800656. https://doi.org/10.1002/adem.201800656

Das, S., 2008. Primary magnesium production costs for automotive applications. JOM. https://doi.org/10.1007/s11837-008-0151-7

Ding, J., Bandak, G., Leen, S.B., Williams, E.J., Shipway, P.H., 2009. Experimental characterisation and numerical simulation of contact evolution effect on fretting crack nucleation for Ti-6Al-4V. Tribol. Int. 42, 1651–1662. https://doi.org/10.1016/j.triboint.2009.04.040

Froes, F.H., Eliezer, D., Aghion, E., 1998. The science, technology, and applications of magnesium. JOM. https://doi.org/10.1007/s11837-998-0411-6

Graff, S., Brocks, W., Steglich, D., 2007. Yielding of magnesium: From single crystal to polycrystalline aggregates. Int. J. Plast. 23, 1957–1978. https://doi.org/10.1016/j.ijplas.2007.07.009

Grogan, J.A., Leen, S.B., McHugh, P.E., 2014. Computational micromechanics of bioabsorbable magnesium stents. J. Mech. Behav. Biomed. Mater. 34, 93–105. https://doi.org/10.1016/j.jmbbm.2014.01.007

Grogan, J.A., O'brien, B.J., Leen, S.B., Mchugh, P.E., 2011. A corrosion model for bioabsorbable metallic stents. Acta Biomater. 7, 3523–3533. https://doi.org/10.1016/j.actbio.2011.05.032

Huang, Y., 1991. A USER-MATERIAL SUBROUTINE INCORPORATING SINGLE CRYSTAL PLASTICITY IN THE ABAQUS FINITE ELEMENT PROGRAM A USER-MATERIAL SUBROUTINE INCORPORATING SINGLE CRYSTAL

PLASTICITY IN THE ABAQUS FINITE ELEMENT PROORAM.

Kirchhoff, C., Braunstein, V., Kirchhoff, S., Sprecher, C.M., Ockert, B., Fischer, F., Leidel, B.A., Biberthaler, P., 2008. Outcome analysis following removal of locking plate fixation of the proximal humerus. BMC Musculoskelet. Disord. https://doi.org/10.1186/1471-2474-9-138

Kulekci, M.K., 2008. Magnesium and its alloys applications in automotive industry. Int. J. Adv. Manuf. Technol. 39, 851–865. https://doi.org/10.1007/s00170-007-1279-2

Li, H., Lv, F., Xiao, Z., Liang, X., Sang, F., Li, P., 2016. Low-cycle fatigue behavior of a cast Mg–Y–Nd–Zr alloy by T6 heat treatment. Mater. Sci. Eng. A 676, 377–384. https://doi.org/10.1016/j.msea.2016.09.001

Ligier, J.N., Metaizeau, J.P., Prevot, J., Lascombes, P., 1988. Elastic stable intramedullary nailing of femoral shaft fractures in children. J. Bone Jt. Surg. - Ser. B. https://doi.org/10.1302/0301-620x.70b1.3339064

Manonukul, A., Dunne, F.P.E., 2004. High- and low-cycle fatigue crack initiation using polycrystal plasticity. Proc. R. Soc. A Math. Phys. Eng. Sci. 460, 1881–1903. https://doi.org/10.1098/rspa.2003.1258

McCarthy, O.J., McGarry, J.P., Leen, S.B., 2014. The effect of grain orientation on fretting fatigue plasticity and life prediction. Tribology International, 76, 100–115. https://doi.org/10.1016/j.triboint.2013.09.023

McCarthy, O.J., McGarry, J.P., Leen, S.B., 2014b. Micro-mechanical modelling of fretting fatigue crack initiation and wear in Ti-6Al-4V. Int. J. Fatigue. 62, 180–193. https://doi.org/10.1016/j.ijfatigue.2013.04.019

McCarthy, O.J., McGarry, J.P., Leen, S.B., 2013. Microstructure-sensitive prediction and experimental validation of fretting fatigue. Wear. 305 (1-2), 100-114. https://doi.org/10.1016/j.wear.2013.05.012

McCarthy, O.J., McGarry, J.P., Leen, S.B., 2011. A finite element study of microstructure-sensitive plasticity and crack nucleation in fretting. Comput. Mater. Sci. 50, 2439–2458. https://doi.org/10.1016/j.commatsci.2011.03.026

McGarry, J.P., O'Donnell, B.P., McHugh, P.E., McGarry, J.G., 2004. Analysis of the mechanical performance of a cardiovascular stent design based on micromechanical modelling. Comput. Mater. Sci. 31, 421–438. https://doi.org/10.1016/j.commatsci.2004.05.001

McGarry, J.P., O'Donnell, B.P., McHugh, P.E., O'Cearbhaill, E., McMeeking, R.M., 2007. Computational examination of the effect of material lnhomogeneity on the necking of stent struts under tensile loading. Journal of Applied Mechanics, 74 (5), 978-989. https://doi.org/10.1115/1.2722776

McGhee, P.R., 2017. Effect of Microstructure on the Mechanical Properties of Extruded Magnesium and a Magnesium Alloy.

Mirza, F., Zhang, D.C.-A.M.H., S, U., 2013, U., 2013. Fatigue of magnesium alloys. academia.edu.

Mirza, F.A., Chen, D.L., 2014. Fatigue of rare-earth containing magnesium alloys: a review. Fatigue Fract. Eng. Mater. Struct. 37, 831–853. https://doi.org/10.1111/ffe.12198

Mirza, F.A., Chen, D.L., Li, D.J., Zeng, X.Q., 2014. Low cycle fatigue of an extruded Mg-3Nd-0.2Zn-0.5Zr magnesium alloy. Mater. Des. 64, 63–73. https://doi.org/10.1016/j.matdes.2014.07.016

Mirza, F.A., Chen, D.L., Li, D.J., Zeng, X.Q., 2013. Low cycle fatigue of a rare-earth containing extruded magnesium alloy. Mater. Sci. Eng. A 575, 65–73. https://doi.org/10.1016/j.msea.2013.03.041

Mishra, R.K., Gupta, A.K., Rao, P.R., Sachdev, A.K., Kumar, A.M., Luo, A.A., 2008. Influence of cerium on the texture and ductility of magnesium extrusions. Scr. Mater. 59, 562–565. https://doi.org/10.1016/j.scriptamat.2008.05.019

Mordike, B.L., Ebert, T., 2001. Magnesium Properties - applications - potential. Mater. Sci. Eng. A 302, 37–45. https://doi.org/10.1016/S0921-5093(00)01351-4

Narayanan, U.G., Hyman, J.E., Wainwright, A.M., Rang, M., Alman, B.A., 2004. Complications of elastic stable intramedullary nail fixation of pediatric femoral fractures, and how to avoid them. J. Pediatr. Orthop. https://doi.org/10.1097/01241398-200407000-00004

Nørgaard, S.L., Riber, S.S., Danielsson, F.B., Pedersen, N.W., Viberg, B., 2018. Surgical approach for elastic stable intramedullary nail in pediatric radius shaft fracture: A systematic review. J. Pediatr. Orthop. Part B.

https://doi.org/10.1097/BPB.0000000000000458

Shahzad, M., Wagner, L., 2009. Influence of extrusion parameters on microstructure and texture developments, and their effects on mechanical properties of the magnesium alloy AZ80. Mater. Sci. Eng. A 506, 141–147. https://doi.org/10.1016/j.msea.2008.11.038

Teoh, S., 2000. Fatigue of biomaterials: a review. Int. J. Fatigue 22, 825–837. https://doi.org/10.1016/S0142-1123(00)00052-9

Wang, F., Dong, J., Jiang, Y., Ding, W., 2013. Cyclic deformation and fatigue of extruded Mg-Gd-Y magnesium alloy. Mater. Sci. Eng. A 561, 403–410. https://doi.org/10.1016/j.msea.2012.10.048

Zhao, D., Witte, F., Lu, F., Wang, J., Li, J., Qin, L., 2017. Current status on clinical applications of magnesium-based orthopaedic implants: A review from clinical translational perspective. Biomaterials. https://doi.org/10.1016/j.biomaterials.2016.10.017